Waves produced from a harmonic point source in a supersonic boundary-layer flow

By P. BALAKUMAR AND M. R. MALIK

High Technology Corporation, PO Box 7262, Hampton VA 23666, USA

The disturbance wave pattern produced from a harmonic point source in a compressible flat-plate boundary layer is computed using linear stability theory and the direct numerical integration approach. Receptivity coefficients are computed for a wide band of least-stable spanwise modes generated at the source, which are followed in the streamwise direction in order to study the wave-interference pattern. The effect of boundary-layer growth on the development of linear waves is determined by using the method of multiple scales. Results are presented for Mach numbers of 0, 2 and 7. It is found that disturbances spread in wedge-shaped regions behind the source and the wedge angle decreases with Mach number. The lateral spreading angle for the instability waves turns out to be quite close to the angle found experimentally for lateral contamination of turbulence. It is found that, owing to wave cancellation, the computed maximum disturbance amplitude is significantly lower than that obtained by following the most-amplified single normal mode.

1. Introduction

In natural transition the spectra of the disturbances which are internalized in the boundary layer have a wide band of frequencies and spanwise wavenumbers. When these disturbances evolve downstream, they are amplified differently depending upon the frequency, spanwise wavenumber and Reynolds number. Since the Reynolds number varies in the streamwise direction, the identity of the most amplified wave also changes in the downstream direction. Hence, there is no single wave which will remain dominant in the entire downstream. Furthermore, if the waves with different spanwise wavenumbers are phase related, then their mutual interference will influence the amplitude of the disturbances, unlike predictions which are based on considering only single waves. For low-speed flow, it was clearly demonstrated by the wavepacket experiment of Gaster & Grant (1975) and calculations of Gaster (1982) that the maximum amplitude in the wavepacket does not grow even though the single normal mode grows exponentially.

In this paper, we investigate the propagation of disturbances in a supersonic boundary layer. The disturbances are introduced from a localized harmonic point source. Thus, a wide band of spanwise wavenumbers is excited at the source, but, in contrast with the wavepacket experiment, a single frequency is present, namely the frequency of the excitation of the source. This problem can be considered as a model for studying the boundary-layer instability waves which are generated at isolated roughness sites or surface imperfections because of interaction with free-stream disturbances of a given frequency.

When a localized disturbance is introduced into a flow field, the disturbance field

can be divided into two regions. One region is near the source and the other is further downstream of the source. The flow field in the near-field region, which consists of all the discrete modes and a continuous spectrum, was recently studied by Balakumar & Malik (1992) (referred herein as BM). We found that the continuous spectrum, which appears due to the boundary conditions at the edge of the boundary layer, decays algebraically away from the source. Hence, any contribution from the continuous spectrum can be neglected in the far field. Among the discrete eigenvalues, only one may be unstable and grow exponentially downstream of the source, and all the others will decay exponentially. Therefore, the disturbances in the far field consist of these exponentially growing discrete eigensolutions, which are the subject of this paper. Thus, we first compute the receptivity coefficient for the discrete eigenvalues using the approach adopted in BM. In the second step, we follow the evolution of the least-stable eigenmodes in a growing boundary layer using multiple-scales analysis. We note that this procedure can be adopted for a more general problem than a point-source case. We basically use the harmonic point source to model the external disturbance and to get the associated receptivity coefficient.

Several experiments have been done on the harmonic point source problem in incompressible and compressible boundary-layer flows. Gilev, Kachanov & Kozlov (1981) performed a detailed experiment in an essentially incompressible flow. They used hot-wire measurements to determine the amplitude and the phase distributions of the streamwise disturbance velocity downstream of the source. From this data they mapped out the constant phase lines and calculated the Fourier spectrum of the disturbance velocity at different streamwise cross-sections. Mack & Kendall (1983) and Mack (1985) investigated this problem experimentally as well as numerically. Kosinov & Maslov (1985) and Kosinov, Maslov & Shevelkov (1990) performed experiments on the point-source problem in compressible flow. Using Fourier analysis they were able to determine the amplification rates of normal-mode disturbances. However, they could not measure the amplification rates of the waves at small wave angles. Their experiment was performed in a 'noisy' wind tunnel and it is difficult to discern the effect wind tunnel noise had on their results. We shall compare our numerical results with the experiments of Gilev *et al.* (1981).

In §2, we formulate the problem when the mean flow is uniform in the streamwise direction. The parallel-flow approximation is made for the determination of the receptivity coefficient. In §3, a formulation is given for the evolution of the least-stable discrete modes propagating downstream in a growing boundary layer. Results are presented in §4 and conclusions are drawn in §5.

2. Receptivity problem

We consider two-dimensional, compressible boundary-layer flow over an insulated flat plate. A harmonic point source of disturbances is embedded in the wall at a streamwise location $x = x_0$ (see figure 1). The distance normal to the plate is measured by coordinate y while z represents the spanwise coordinate. The x, y, z components of velocity are represented by U, V, W, respectively, and pressure, density and temperature of the gas by P, ρ, T. The corresponding disturbance quantities are denoted by $(u, v, w, p, \tau, \theta)$. We are interested in the response of the boundary layer to a three-dimensional harmonic excitation of the point source starting impulsively at time $t = 0$. In this section we assume that the basic flow is parallel to the x-axis $(U(y), 0, 0, P(y), \rho(y), T(y))$ and determine the receptivity coefficients for the various modes. We will treat non-parallel effects in the next

$$U_\infty, T_\infty$$

$$x = x_0$$

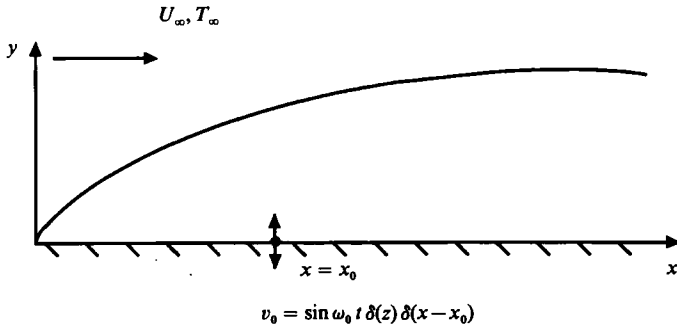$$v_0 = \sin \omega_0 t\, \delta(z)\, \delta(x - x_0)$$

FIGURE 1. A schematic of the harmonic point source embedded in the flat plate.

section where we consider the development of the disturbances downstream of the source. The linearized, non-dimensionalized Navier–Stokes, energy, continuity and state equations for a fluid with dynamic viscosity μ are

$$\rho\left(\frac{\partial u}{\partial t} + U\frac{\partial u}{\partial x} + v\frac{dU}{dy}\right) = -\frac{\partial p}{\partial x} + \frac{1}{\mathrm{Re}}\left[2\mu\frac{\partial^2 u}{\partial x^2} + \mu\left(\frac{\partial^2 u}{\partial y^2} + \frac{\partial^2 u}{\partial z^2} + \frac{\partial^2 v}{\partial x\,\partial y} + \frac{\partial^2 w}{\partial x\,\partial z}\right)\right.$$

$$\left. - \tfrac{2}{3}\mu\left(\frac{\partial^2 u}{\partial x^2} + \frac{\partial^2 v}{\partial x\,\partial y} + \frac{\partial^2 w}{\partial x\,\partial z}\right) + \frac{d\mu}{dT}\frac{dT}{dy}\left(\frac{\partial u}{\partial y} + \frac{\partial v}{\partial x}\right) + \frac{d\mu}{dT}\left(\frac{d^2 U}{dy^2}\theta + \frac{dU}{dy}\frac{\partial\theta}{\partial y}\right) + \frac{d^2\mu}{dT^2}\frac{dT}{dy}\frac{dU}{dy}\theta\right],$$

(2.1)

$$\rho\left(\frac{\partial v}{\partial t} + U\frac{\partial v}{\partial x}\right) = -\frac{\partial p}{\partial y} + \frac{1}{\mathrm{Re}}\left[2\mu\frac{\partial^2 v}{\partial y^2} + \mu\left(\frac{\partial^2 v}{\partial x^2} + \frac{\partial^2 v}{\partial z^2} + \frac{\partial^2 u}{\partial x\,\partial y} + \frac{\partial^2 w}{\partial y\,\partial z}\right)\right.$$

$$\left. - \tfrac{2}{3}\mu\left(\frac{\partial^2 u}{\partial x\,\partial y} + \frac{\partial^2 v}{\partial y^2} + \frac{\partial^2 w}{\partial y\,\partial z}\right) + \frac{d\mu}{dT}\left(2\frac{dT}{dy}\frac{\partial v}{\partial y} + \frac{dU}{dy}\frac{\partial\theta}{\partial x}\right) - \frac{2}{3}\frac{d\mu}{dT}\frac{dT}{dy}\left(\frac{\partial u}{\partial x} + \frac{\partial v}{\partial y} + \frac{\partial w}{\partial z}\right)\right],$$

(2.2)

$$\rho\left(\frac{\partial w}{\partial t} + U\frac{\partial w}{\partial x}\right) = -\frac{\partial p}{\partial z} + \frac{1}{\mathrm{Re}}\left[2\mu\frac{\partial^2 w}{\partial z^2} + \mu\left(\frac{\partial^2 w}{\partial y^2} + \frac{\partial^2 w}{\partial x^2} + \frac{\partial^2 v}{\partial y\,\partial z} + \frac{\partial^2 u}{\partial x\,\partial z}\right)\right.$$

$$\left. - \tfrac{2}{3}\mu\left(\frac{\partial^2 w}{\partial z^2} + \frac{\partial^2 v}{\partial y\,\partial z} + \frac{\partial^2 u}{\partial x\,\partial z}\right) + \frac{d\mu}{dT}\frac{dT}{dy}\left(\frac{\partial w}{\partial y} + \frac{\partial v}{\partial z}\right)\right],$$

(2.3)

$$\rho\left(\frac{\partial\theta}{\partial t} + U\frac{\partial\theta}{\partial x} + v\frac{dT}{dy}\right) = -(\gamma-1)\left(\frac{\partial u}{\partial x} + \frac{\partial u}{\partial y} + \frac{\partial w}{\partial z}\right) + \frac{\gamma}{\sigma\,\mathrm{Re}}\left[\mu\left(\frac{\partial^2\theta}{\partial x^2} + \frac{\partial^2\theta}{\partial y^2} + \frac{\partial^2\theta}{\partial z^2}\right) + \frac{d\mu}{dT}\frac{d^2 T}{dy^2}\theta\right.$$

$$\left. + 2\frac{d\mu}{dT}\frac{dT}{dy}\frac{\partial\theta}{\partial y} + \frac{d^2\mu}{dT^2}\left(\frac{dT}{dy}\right)^2\theta\right] + \frac{\gamma(\gamma-1)}{\mathrm{Re}}M^2\left[2\mu\frac{dU}{dy}\left(\frac{\partial u}{\partial y} + \frac{\partial v}{\partial x}\right) + \frac{d\mu}{dT}\left(\frac{dU}{dy}\right)^2\theta\right],$$

(2.4)

$$\frac{\partial\tau}{\partial t} + \rho\left(\frac{\partial u}{\partial x} + \frac{\partial v}{\partial y} + \frac{\partial w}{\partial z}\right) + v\frac{d\rho}{dy} + U\frac{\partial\tau}{\partial x} = 0,$$

(2.5)

$$\gamma M^2 p = \rho\theta + \tau T.$$

(2.6)

Here the variables are non-dimensionalized as follows:

velocity by U_∞, temperature by T_∞, density by ρ_∞, (2.7a)

pressure by $\rho_\infty U_\infty^2$, length by $(\nu_\infty x_0/U_\infty)^{\frac{1}{2}}$, time by $(\nu_\infty x_0)^{\frac{1}{2}}/U_\infty^{\frac{3}{2}}$, (2.7b)

where $U_\infty, T_\infty, \rho_\infty, P_\infty, \nu_\infty$ are free-stream velocity, temperature, density, pressure and kinematic viscosity. Stokes' hypothesis of vanishing bulk viscosity has been used here. The non-dimensional quantities appearing in the equations are defined as

M = free-stream Mach number, $U_\infty/(\gamma \Re T_\infty)^{\frac{1}{2}}$,

σ = Prandtl number, assumed to be a constant value of 0.72,

γ = specific heat ratio, taken as 1.4,

Re = Reynolds number, $(U_\infty x_0/\nu_\infty)^{\frac{1}{2}}$,

$\Re$ = gas constant.

The boundary conditions at the wall are $u = \theta = w = 0$ and

$$u(x, 0, z, t) = \sin \omega_0 \tau\, \delta(x - x_0)\, \delta(z)\, H(t), \tag{2.8}$$

where ω_0 is the frequency of oscillation of the point source, δ is Dirac's delta function and $H(t)$ is the unit step function, which indicates that the motion starts from rest at $t = 0$. We require that the disturbances decay far away from the plate.

The physical disturbance field may be related to the spectral space by using the generalized triple Fourier transform defined as

$$\tilde{\phi}(k_x, y, k_z, \omega) = \int_{-\infty}^{\infty} \mathrm{d}t \int_{-\infty}^{\infty} \mathrm{d}x \int_{-\infty}^{\infty} \mathrm{d}z\, \phi(x, y, z, t)\, \mathrm{e}^{-\mathrm{i}(k_x x + k_z z - \omega t)}, \tag{2.9}$$

where k_x, k_z are the complex wavenumbers in the x, z-directions, ω is the complex frequency, $\phi = \{u, v, w, \theta, p\}^{\mathrm{T}}$, and $\tilde{\phi} = \{\tilde{u}, \tilde{v}, \tilde{w}, \tilde{\theta}, \tilde{p}\}^{\mathrm{T}}$. Here, the tilde represents the transformed variable and superscript T represents the transpose of a matrix. Since ϕ is a causal function in t, the Fourier transform in time is equivalent to the Laplace transform in time. Thus (2.1)–(2.6) can be transformed using (2.9) into the following system of equations for $\tilde{\phi}$:

$$\boldsymbol{A} \frac{\mathrm{d}^2 \tilde{\phi}}{\mathrm{d}y^2} + \boldsymbol{B} \frac{\mathrm{d}\tilde{\phi}}{\mathrm{d}y} + \boldsymbol{C}\tilde{\phi} = 0, \tag{2.10}$$

where $\boldsymbol{A}, \boldsymbol{B}, \boldsymbol{C}$ are 5×5 matrices whose coefficients are given in Malik (1990). Transforming the boundary conditions yields

$$\tilde{v}(k_x, 0, k_z, \omega) = -\omega_0/(\omega^2 - \omega_0^2), \tag{2.11}$$

$$\tilde{u} = \tilde{w} = \tilde{\theta} = 0 \quad \text{at} \quad y = 0, \tag{2.12}$$

$$\text{and } \tilde{\phi} \text{ is bounded as } y \to \infty. \tag{2.13}$$

By taking the inverse transformations it can be shown (BM) that the solution takes the form

$$\phi(x, y, z, t) = \frac{1}{2\pi} \int_{-\infty}^{\infty} \mathrm{e}^{\mathrm{i}k_z z}\, \mathrm{Re}\,[I]\, \mathrm{d}k_z, \tag{2.14}$$

where $\qquad I = \sum \mathrm{i}C(k_z, \omega_0)\, \boldsymbol{\psi}(k_x, y, k_z)\, \mathrm{e}^{\mathrm{i}k_x(\omega_0)x - \mathrm{i}\omega_0 t} + \sum V_{\mathrm{B}}(x, y, k_z)\, \mathrm{e}^{-\mathrm{i}\omega_0 t}, \tag{2.15}$

where $\boldsymbol{\psi}$ is the eigenfunction, C is the receptivity coefficient for the discrete mode, and V_{B} is the contribution from the continuous spectrum. The receptivity coefficient C is determined from the formula

$$C = \mathrm{i}/\boldsymbol{\psi}(k_x, y, k_z, \omega_0) \frac{\partial}{\partial k_x} \frac{1}{\tilde{\phi}}\bigg|_{k_x(\omega_0)}, \tag{2.16}$$

where $\hat{\phi}$ is a five-element vector $\{\hat{u}, \hat{v}, \hat{w}, \hat{\theta}, \hat{p}\}^T$ which is determined by solving the non-homogeneous stability problem similar to (2.10)–(2.13) with the boundary condition (2.11) modified to $\hat{v}(y = 0) = 1$. The reader is referred to BM for further details for determination of the receptivity coefficient.

3. Disturbance evolution in the growing boundary layer

In the previous section we assumed that the mean flow quantities are a function of normal coordinate y only. This permits us to analyse the problem using transform techniques. The solution consists of two parts: all the discrete modes; and the contribution from the continuous spectrum. The continuous spectrum decays slowly in the streamwise direction. Hence, sufficiently downstream of the source we see the discrete unstable eigenmode. In this section we investigate the downstream evolution of the most unstable discrete modes and allow for the effect of boundary-layer growth.

In the previous section we derived that the disturbance emanating from the point source is given by (2.14) and (2.15). Since the continuous spectrum and the higher discrete modes decay in the downstream direction, only the discrete least-stable mode will contribute to the flow field far downstream. Hence, the flow field downstream takes the form

$$\phi(x, y, z, t) = \frac{1}{2\pi} \int_{-\infty}^{\infty} e^{ik_z z} \operatorname{Re} \{\tilde{\tilde{I}}(x_0, y, k_z, t)\} \, dk_z, \tag{3.1}$$

where

$$\tilde{\tilde{I}} = iC(k_z, \omega_0) \, \tilde{\psi}(k_z, y) \, e^{ik_x(\omega_0)x} \, e^{-i\omega_0 t}, \tag{3.2}$$

and $k_x(\omega_0)$ is the least-stable discrete eigenmode. Here, the integral (3.1) will be evaluated along the real k_z axis. In a growing boundary layer the expression for $\tilde{\tilde{I}}$ is modified to

$$\tilde{\tilde{I}} = iA(x, \omega_0, k_z) \, \psi(y, x, \omega_0, k_z, \alpha) \exp\left[\int_{x_0}^{x} i\alpha(\omega_0, k_z, x) \, dx - i\omega_0 t\right]. \tag{3.3}$$

Here $\psi(y, x, \omega_0, k_z, \alpha)$ is the eigenfunction at the station x and $\alpha(\omega_0, k_z, x)$ is the eigenvalue (complex streamwise wavenumber) at the station x. $A(x, \omega_0, k_z)$ is a slowly varying function of x and

$$A(x = x_0, \omega_0, k_z) = C(k_z, \omega_0). \tag{3.4}$$

We can derive an amplitude equation for $A(x, \omega_0, k_z)$ using multiple-scales analysis (Saric & Nayfeh 1975; Gapanov 1981; El-Hady 1991). In the following we describe the theory.

3.1. *Multiple-scales analysis*

In this section we find the non-parallel correction to the quasi-parallel compressible linear stability problem using the multiple-scales analysis. The assumption behind this approach is that the mean boundary-layer flow quantities vary slowly in the streamwise direction compared to the disturbance quantities. This introduces two lengthscales: the long scale which is the length over which mean flow quantities vary, and the short scale which is the length over which disturbance quantities vary. In the multiple-scales analysis, these two lengthscales are treated as independent variables and solution is obtained by applying the solvability condition.

Here, in contrast with §2, mean boundary-layer flow quantities (U, V, P, ρ, T) are functions of both x and y. Thus the relevant linearized Navier–Stokes, energy and

continuity equations differ from (2.1)–(2.5) in that they contain terms such as $V, \partial U/\partial x, \partial T/\partial x$, etc. These equations are given in Malik (1990). Here the flow quantities are non-dimensionalized as in (2.7) except that the analysis is performed at a location x_1^* (the superscript * implies dimensional length). Therefore, the local lengthscale is $(\nu_\infty x_1^*/u_\infty)^{\frac{1}{2}}$ and Reynolds number Re is $(u_\infty x_1^*/\nu_\infty)^{\frac{1}{2}}$. We assume that the disturbances vary with the lengthscale $(\nu_\infty x_1^*/U_\infty)^{\frac{1}{2}}$ and the mean flow quantities vary with the long lengthscale x_1^*. We define a slow scale $\chi = \epsilon x$, where ϵ is a small parameter equal to $1/Re$. Therefore, the mean flow quantities are functions of χ and y:

$$U(x,y) = U(\chi,y), \quad V(x,y) = V(\chi,y), \quad T(x,y) = T(\chi,y), \quad \rho(x,y) = \rho(\chi,y).$$

We seek solutions to the linearized Navier–Stokes equations of the form

$$q(x,y,z,t) = A(\chi)(q_0(\chi,y) + \epsilon q_1(\chi,y) + O(\epsilon^2)) \exp\left[i\frac{S_0(\chi)}{\epsilon} + O(\epsilon) - i\omega_0 t + ik_z z \right], \quad (3.5)$$

where q is a vector $\{u,v,w,\theta,p,\tau\}^{\mathrm{T}}$ and q_i is a vector $\{u_i, v_i, w_i, \theta_i, p_i, \tau_i\}^{\mathrm{T}}$ which are functions of χ and y, and $S_0(\chi)$ is a phase function which is a function of χ only. The amplitude function $A(\chi)$ is also a function of χ only. Substituting (3.5) into the linearized Navier–Stokes equations and collecting terms of the same order in ϵ we obtain the following system of equations:

Order ϵ^0

$$L_i(q_0) = 0; \quad i = 1, \ldots, 6, \qquad (3.6)$$

Order ϵ^1

$$L_i(q_1) = \frac{1}{A(\chi)} \frac{\mathrm{d}A}{\mathrm{d}\chi} R_{1i} + R_{2i}; \quad i = 1, \ldots, 6, \qquad (3.7)$$

where L_i, R_{1i}, R_{2i} $(i = 1, 6)$ are given in an Appendix.† The boundary conditions are

$$u_i, v_i, w_i, \theta_i = 0 \quad \text{at} \quad y = 0, \qquad (3.8a)$$

and
$$u_i, v_i, w_i, \theta_i \to 0 \quad \text{when} \quad y \to \infty. \qquad (3.8b)$$

We observe that the leading-order equations are the linear stability equations for a parallel flow and give the eigensolutions q_0 and $\alpha_0 = \mathrm{d}S_0/\mathrm{d}\chi$. The higher-order equations are non-homogeneous equations in which the operator on the left-hand side is the compressible linear stability operator while the right-hand side contains the non-parallel terms.

3.2. *Solution procedure*

First we reduce the system of equations (3.6)–(3.7) to a system of first-order equations. This yields the following:

Order ϵ^0

$$\frac{\partial \psi_0}{\partial y} = B\psi_0, \qquad (3.9)$$

Order ϵ^1

$$\frac{\partial \psi_1}{\partial y} = B\psi_1 + \frac{1}{A(\chi)} \frac{\mathrm{d}A}{\mathrm{d}\chi} Q_1 + Q_2. \qquad (3.10)$$

† The Appendix is available on request from the Editorial Office or the author.

Here $\boldsymbol{\psi}_i = \{u_i, \partial u_i/\partial y, v_i, p_i, \theta_i, \partial\theta_i/\partial y, w_i, \partial w_i/\partial y\}^{\mathrm{T}}$ is an eight-element vector and $\boldsymbol{B}$ is an 8×8 matrix derived from (3.6); $\boldsymbol{Q}_1$ and $\boldsymbol{Q}_2$ are eight-element column vectors derived from R_{1i} and R_{2i}, respectively. The boundary conditions are

$$u_i = v_i = \theta_i = w_i = 0 \quad \text{at} \quad y = 0, \tag{3.11a}$$

and
$$u_i, v_i, \theta_i, w_i \to 0 \quad \text{as} \quad y \to \infty. \tag{3.11b}$$

The order-ϵ^0 equations, (3.9), give $\boldsymbol{\psi}_0$ and α_0, which are the eigensolutions of the linear parallel-flow stability equations. The homogeneous part of the order-ϵ^1 equations is the same eigensystem as the $O(\epsilon^0)$ equations. Hence, to have a solution to the inhomogeneous equation (3.10), the inhomogeneous part has to satisfy a solvability condition. This condition takes the form

$$\int_0^\infty \boldsymbol{\psi}_0^{*\mathrm{T}} \left(\frac{1}{A(\chi)} \frac{\mathrm{d}A}{\mathrm{d}\chi} \boldsymbol{Q}_1 + \boldsymbol{Q}_2 \right) \mathrm{d}y = 0, \tag{3.12}$$

where $\boldsymbol{\psi}_0^*$ is the solution of the adjoint of the system (3.9), which can be written as

$$\frac{\partial \boldsymbol{\psi}_0^*}{\partial y} = -[\boldsymbol{B}]^{\mathrm{T}} \boldsymbol{\psi}_0^* \tag{3.13}$$

with the boundary conditions

$$\frac{\partial u_0^*}{\partial y} = \frac{\partial w_0^*}{\partial y} = \frac{\partial \theta_0^*}{\partial y} = p_0^* = 0 \quad \text{at} \quad y = 0 \tag{3.14a}$$

and
$$\frac{\partial u_0^*}{\partial y}, \frac{\partial w_0^*}{\partial y}, \frac{\partial \theta_0^*}{\partial y}, p_0^* \to 0 \quad \text{as} \quad y \to \infty. \tag{3.14b}$$

The solvability condition, (3.12), yields

$$\frac{1}{A(\chi)} \frac{\mathrm{d}A}{\mathrm{d}\chi} = \mathrm{i}\alpha_1(\chi), \tag{3.15}$$

where
$$\alpha_1(\chi) = \mathrm{i} \int_0^\infty \boldsymbol{\psi}_0^{*\mathrm{T}} \boldsymbol{Q}_2 \, \mathrm{d}y \bigg/ \int_0^\infty \boldsymbol{\psi}_0^{*\mathrm{T}} \boldsymbol{Q}_1 \, \mathrm{d}y. \tag{3.16}$$

If we substitute for $A(x, w_0, k_z)$ into (3.3), then for a flat-plate boundary layer (3.3) takes the form

$$\tilde{\tilde{I}} = \mathrm{i}C(k_z, \omega_0, Re_0) \boldsymbol{\psi}_0(y, Re, \omega_0, k_z) \exp\left[2 \int_{Re_0}^{Re} \mathrm{i}\left(\alpha_0 + \frac{1}{Re}\alpha_1 \right) \mathrm{d}Re - \mathrm{i}\omega_0 t \right] \tag{3.17}$$

and (3.1) becomes

$$\phi(x, y, z, t) = \frac{1}{2\pi} \int_{-\infty}^{\infty} \mathrm{e}^{\mathrm{i}k_z z} \operatorname{Re}\left\{ \mathrm{i}C(k_z, \omega_0, Re_0) \boldsymbol{\psi}_0(y, Re, \omega_0, k_z) \right.$$
$$\left. \exp\left[2 \int_{Re_0}^{Re} \mathrm{i}\left(\alpha_0 + \frac{1}{Re}\alpha_1 \right) \mathrm{d}Re \right] - \mathrm{i}\omega_0 t \right\} \mathrm{d}k_z. \tag{3.18}$$

Here Re_0 is the Reynolds number at the location of the point source. In the next section we shall present the results for ϕ obtained from this integral. All the differential equations are solved using the fourth-order-accurate two-point compact scheme of Malik, Chuang & Hussaini (1982).

4. Results

We consider a flat-plate boundary layer with adiabatic wall conditions. The stagnation temperature is taken as 311 K for Mach number 2.0 and is assumed to be 1188 K for $M = 7$. Sutherland's viscosity law is used in the calculations, which are done at three different edge Mach numbers, $M = 0$, 2 and 7. The incompressible calculations were done to compare with the experimental data. These calculations were performed by using the compressible code with an extremely small (but non-zero) Mach number. The harmonic point source is located upstream of the neutral point for the selected frequencies. The Reynolds number (Re_0) at the location of the point source and the non-dimensional frequencies $F = \omega^* \nu_\infty / U_\infty^2$ are given in table 1. Here ω^* is the dimensional frequency and U_∞, ν_∞ are the free-stream velocity and kinematic viscosity, respectively.

The frequencies are selected based on N-factor calculations, i.e. disturbances with these frequencies amplify to significant amplitude ratios. Before we present the results, let us describe the procedure adopted to evaluate the integral in (3.18). We divide the spanwise-wavenumber axis into small sections. For each fixed spanwise wavenumber, k_z, the eigenvalue α_0 and the non-parallel correction α_1 are computed for a range of Reynolds numbers using a two-point fourth-order compact difference scheme. Then the integral in (3.18) is evaluated using linear interpolation between any two grid points along the k_z axis. The integration ranges in the spanwise wavenumber k_z are up to 0.542, 0.448 and 0.106 for $M = 0$, 2 and 7, respectively. The step sizes in k_z are 0.001 at small k_z and are increased to 0.002 at large k_z; and the step size in Reynolds number is 20. The equivalent wave angles at the maximum spanwise wavenumbers are 85°, 89° and 84°. At the high Mach number of 7, the convergence of eigenvalues is very slow at high spanwise wavenumbers and at high Reynolds numbers. Hence, we stopped the calculations at the wave angle given above. Since these eigenvalues are stable at high spanwise wavenumber and at high Reynolds numbers, they will not affect the numerical results except perhaps very close to the source.

Figure 2 shows the receptivity coefficient $C(k_z, \omega_0)$ for the three cases. These receptivity coefficients for the least-stable modes are based upon the maximum amplitude of streamwise velocity fluctuations and are proportional to the amplitude of excitation of the harmonic source. We note that C decreases with Mach number and varies with the spanwise wavenumber k_z.

4.1. *The incompressible case*

Figures 3(a), 4(a), 5 and 6 show the computed results for the incompressible case. Figure 3(a) (plate 1) shows the streamwise velocity u at a time t given by $\omega_0 \tau = 2\nu\pi$, where n is an integer and ω_0 is the non-dimensional frequency (i.e. the signal is periodic with time period $2\pi/\omega_0$) and at height $Y = 1.0$ in the (X, Z)-plane where $X = (x^*/x_0^* - 1)$, $Y = y^*/(\nu_\infty x^*/U_\infty)^{\frac{1}{2}}$ and $Z = z^*/x_0^*$. The scaled value X is related to the Reynolds number through $X = (Re/Re_0)^2 - 1$. Figure 4(a) (plate 2) shows the amplitude of the u-velocity in the (X, Z)-plane at the same height. Figure 5 shows the spanwise variation of the amplitude of the u-velocity at the same height $Y = 1.0$ at different X-locations given by $Re = 605, 705, 805, 905, 1005, 1095$. Figure 5($a$) gives the results with the non-parallel flow correction while figure 5(b) gives the results without this correction, in (3.18). It can be seen that the non-parallel correction not only changes the amplitude at a given Reynolds number, it also affects the distribution of u with z. The kink in the u-distribution at $Z = 0$ and $R = 605$ was also

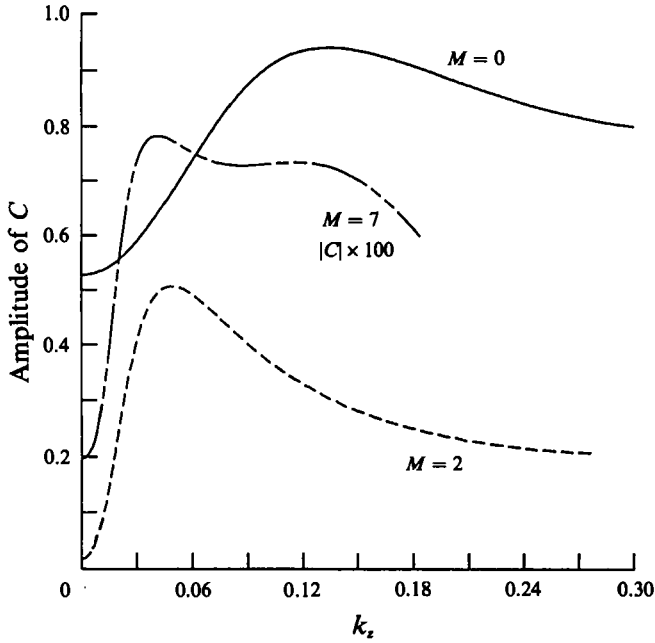| M	Re_0	F
0	485	0.60×10^{-4}
2	900	0.08×10^{-4}
7	300	0.35×10^{-4}

TABLE 1

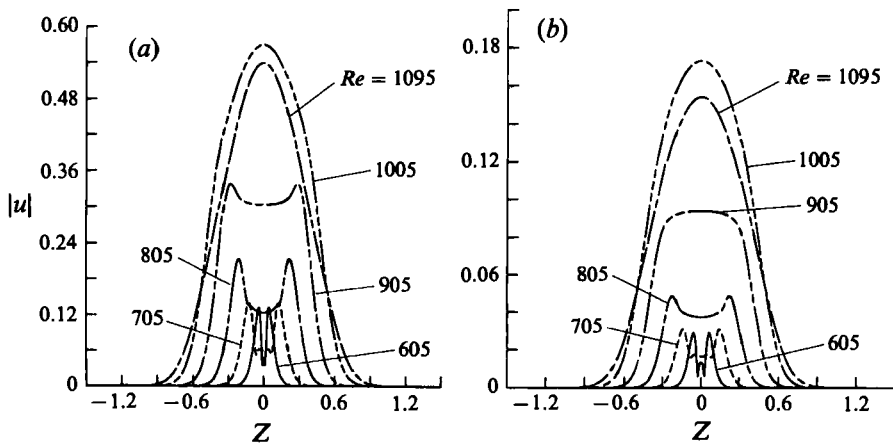FIGURE 2. Variation of the receptivity coefficient for the least-stable mode.

FIGURE 5. Amplitude of the u-velocity at several streamwise locations for the incompressible case: (*a*) non-parallel calculation, (*b*) quasi-parallel flow approximation.
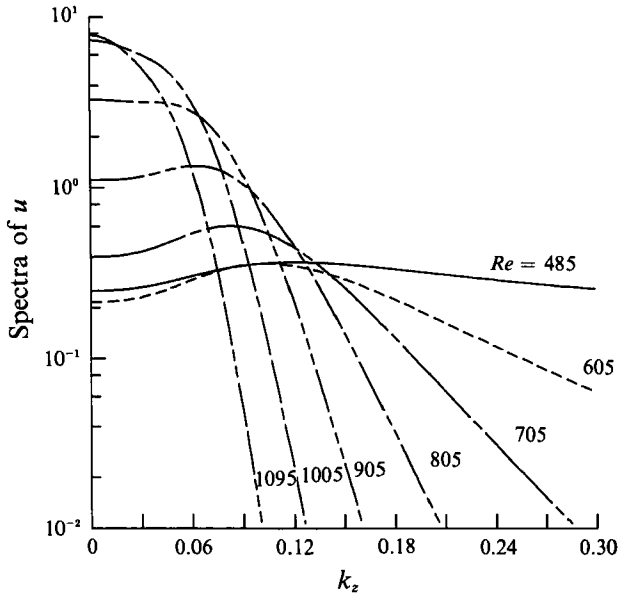
FIGURE 6. Spectra of the u-velocity at several streamwise locations for the incompressible case.

observed in the experiment of Mack & Kendall (1983). In figure 3(*a*), the largest inclination of the constant phase lines is about 50°, i.e. the angle made by the wavenumber vector is 40°. The half spreading angle of the disturbances is about 10°.

Figure 6 shows the spanwise spectrum of the u-velocity at different streamwise locations. We observe that near the source the spectrum is flat and the maximum occurs for a non-zero spanwise wavenumber. This reflects the fact that near the source the maximum amplitude of the disturbances (figure 5) occurs away from the centreline. With increasing Reynolds number the width of the spectrum decreases and the location of the maximum gradually shifts to the zero spanwise wavenumber. The spreading of the disturbances in the spanwise direction and the gradual fading of three-dimensionality which we observed in figures 4(*a*) and 5 correspond to this behaviour.

Gilev *et al.* (1981) performed a comprehensive experiment on the harmonic source problem in an essentially incompressible flow: figure 7 shows their experimental results, where constant phase lines in the (x, z)-plane were mapped out from the hot-wire measurements. It is seen that the wave pattern obtained from the computation (figure 3*a*) agrees very well with these experimental results. Near the source, the maximum amplitude occurs at spanwise locations away from the centreline, due to wave interference, and the constant phase lines are straight lines which meet sharply at the centreline. In the middle region, the sharp crests disappear and the wave pattern becomes flat near the centre. The amplitude in this region is also flat across the spanwise direction (figure 5). In the downstream region, wave fronts assume an arc shape and the maximum amplitude occurs along the centreline. For this frequency, $F = 0.6 \times 10^{-4}$, the maximum amplification occurs for a two-dimensional wave. Hence, when the waves travel downstream, the two-dimensional waves are amplified the most and the three-dimensionality gradually disappears (see figure 6).
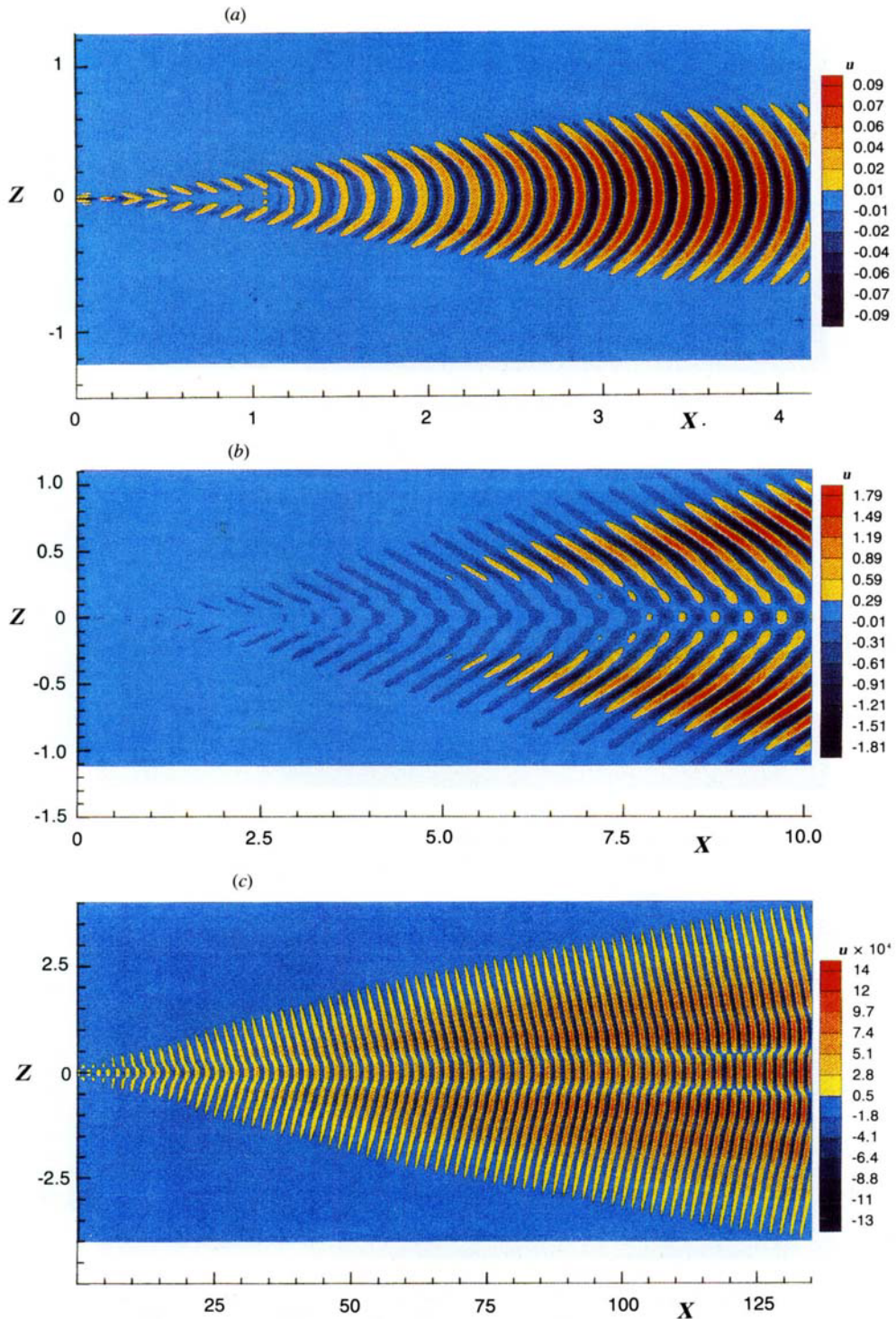
FIGURE 3. Wave pattern produced from a point source for Mach 0, 2 and 7 as observed near the critical layer heights. Here, X is the non-dimensional distance from the source, $X = x^*/x_0^* - 1 = (Re/Re_0)^2 - 1$. $(a)M = 0$, $F = 0.6 \times 10^{-4}$, $Re_0 = 485$; (b) $M = 2$, $F = 0.08 \times 10^{-4}$, $Re_0 = 900$; $(c)M = 7$, $F = 0.35 \times 10^{-4}$, $Re_0 = 300$.
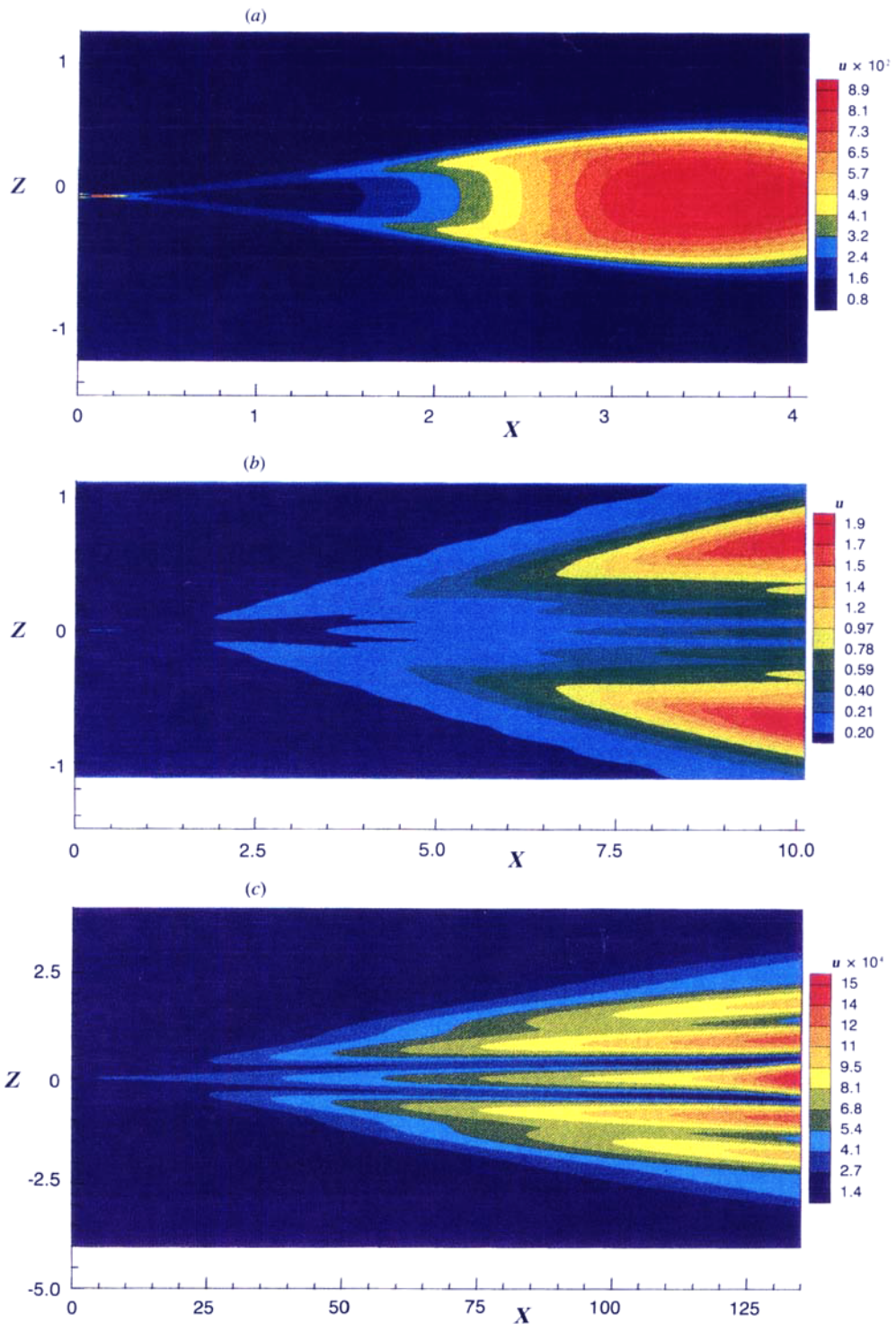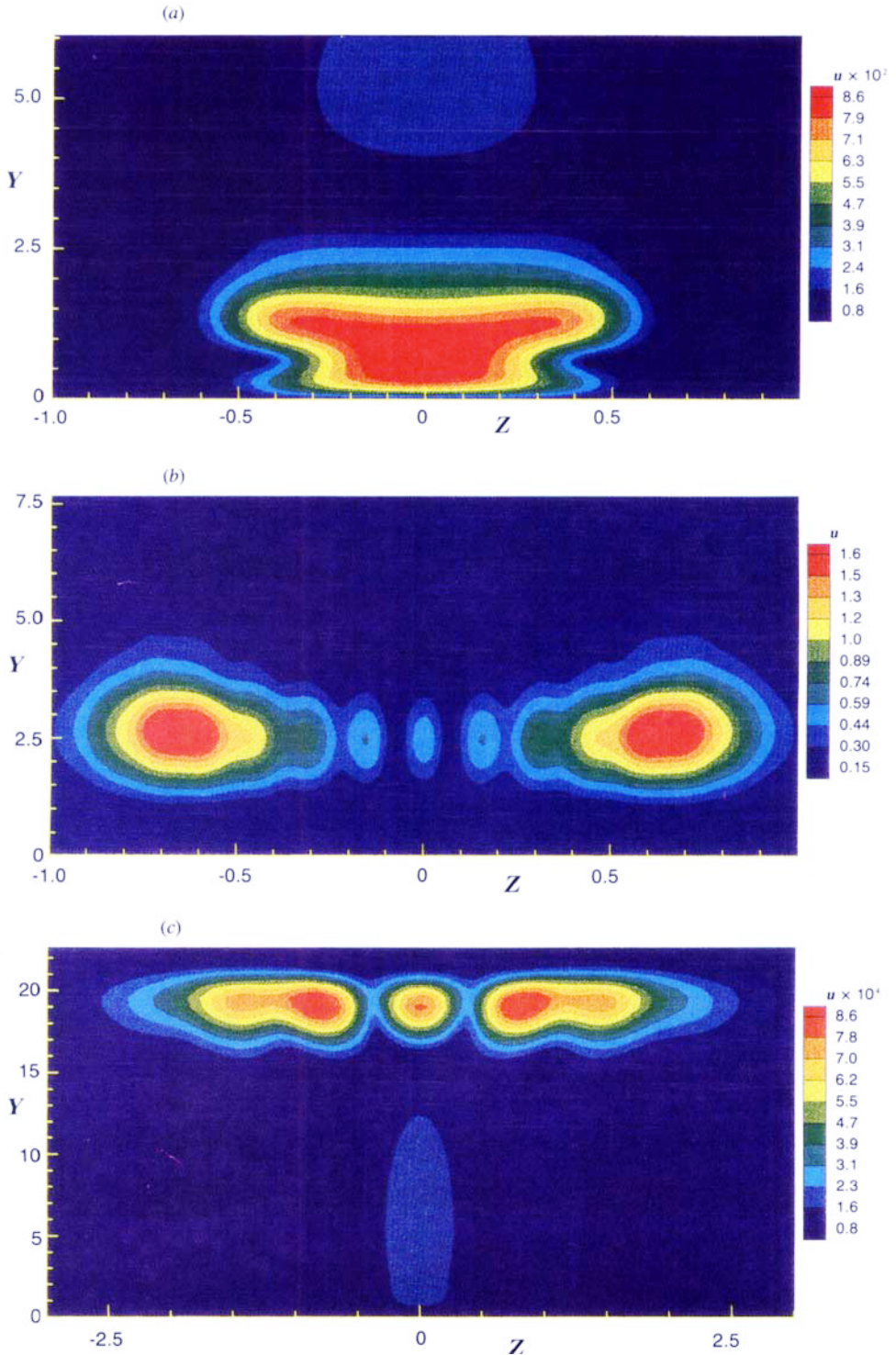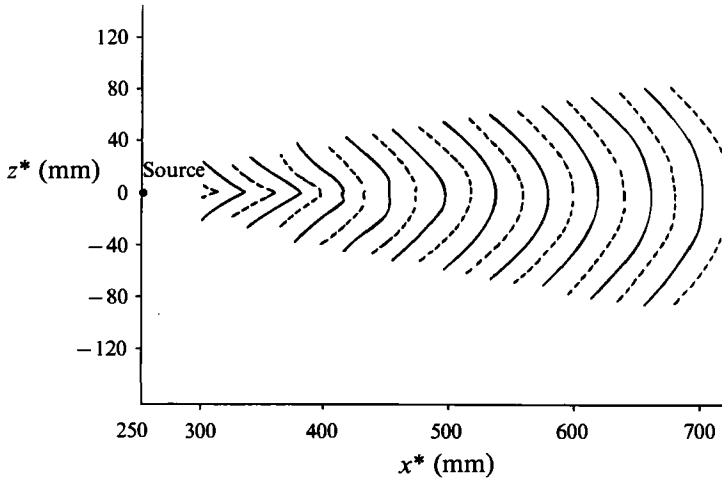
FIGURE 4. Distribution of u-velocity amplitude in the (X,Z)-plane for Mach 0, 2 and 7 at the critical layer heights. $(a)M = 0$, $F = 0.6 \times 10^{-4}$, $Re_0 = 485$; $(b)M = 2$, $F = 0.08 \times 10^{-4}$, $Re_0 = 900$; $(c)M = 7$, $F = 0.35 \times 10^{-4}$, $Re_0 = 300$.

BALAKUMAR & MALIK

FIGURE 16. Distribution of u-velocity amplitude in the (Y,Z)-plane for Mach 0, 2 and 7. $(a) M = 0$, $F = 0.6 \times 10^{-4}$, $Re_0 = 485$, $Re = 1005$; $(b) M = 2$, $F = 0.08 \times 10^{-4}$, $Re_0 = 900$, $Re = 2900$; $(c) M = 7$, $F = 0.35 \times 10^{-4}$, $Re_0 = 300$, $Re = 2900$.

FIGURE 7. Lines of equal phase of disturbances as measured in the experiment of Gilev *et al.* (1981).
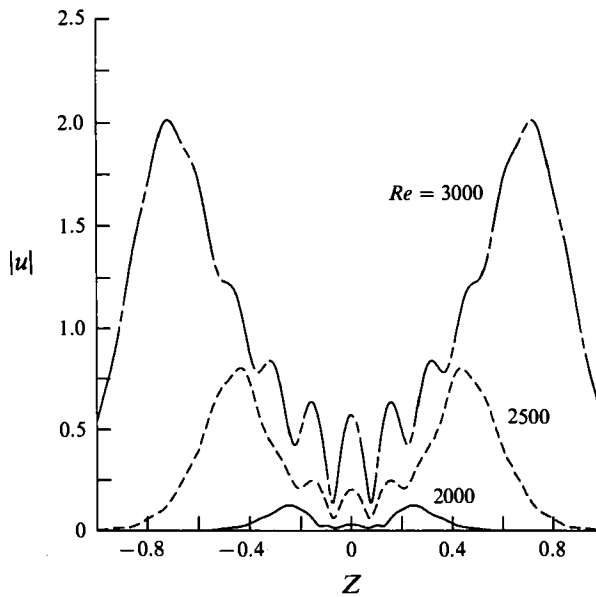
FIGURE 8. Amplitude of the u-velocity at several streamwise locations for the Mach 2 case.

4.2. *The Mach 2 case*

Figures 3(b), 4(b), 8, 9 and 10 show the results for $M = 2$. Figure 3(b) (plate 1) shows the u velocity at a height $Y = 2.68$ in the (X, Z)-plane and at a time t given by $\omega_0 t = 2n\pi$. Figure 4(b) (plate 2) shows the amplitude of the streamwise velocity u in the (X, Z)-plane at the same Y-location. Figure 8 shows the spanwise variation of the amplitude of the u-velocity at the same Y-location and at different X-locations given by $Re = 2000, 2500, 3000$. We see in figures 4(b) and 8 that the disturbances grow in three wedge-shaped regions. One is centred along the X-axis and the other two are centred at oblique angles of $\pm 3.5°$ from the centreline. In the region between these
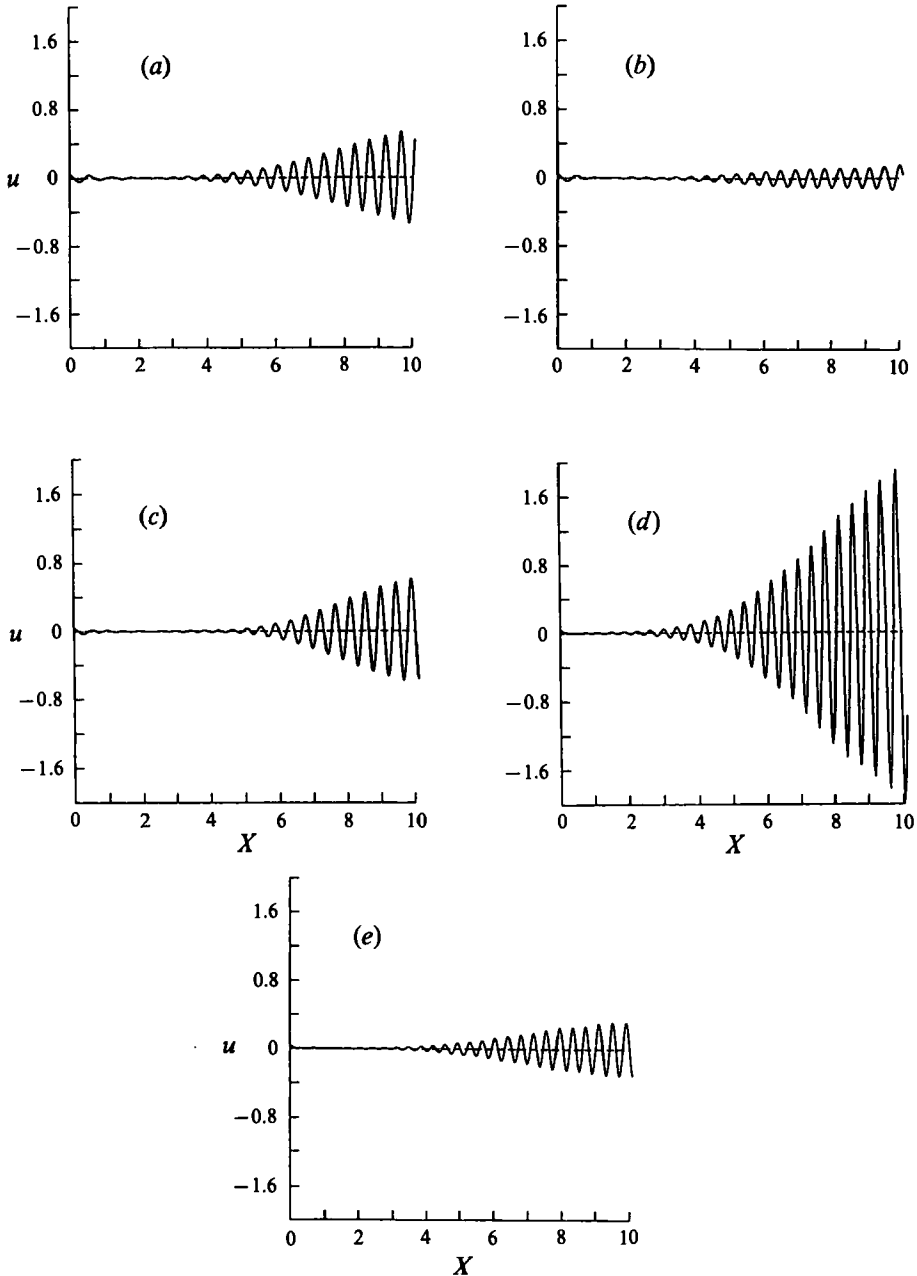
FIGURE 9. Streamwise velocity along lines inclined at various angles to the X-axis for the Mach 2 case: (a) $0°$, (b) $0.5°$, (c) $1°$, (d) $4°$, (e) $6°$.

wedges the disturbance growth is very weak. The constant phase lines (figure 4a) in the most amplified region are inclined at about $25°$ (the wave angle is $65°$). The half spreading angle of the disturbances is about $7°$.

In figure 9, we plot the streamwise velocity u along the lines inclined at 0, $0.5°$, $1°$, $4°$ and $6°$ to the X-axis at the same Y-height and time as given above. We see that the disturbances grow along the $0°$, $1°$ and $4°$ lines but they grow only slightly along
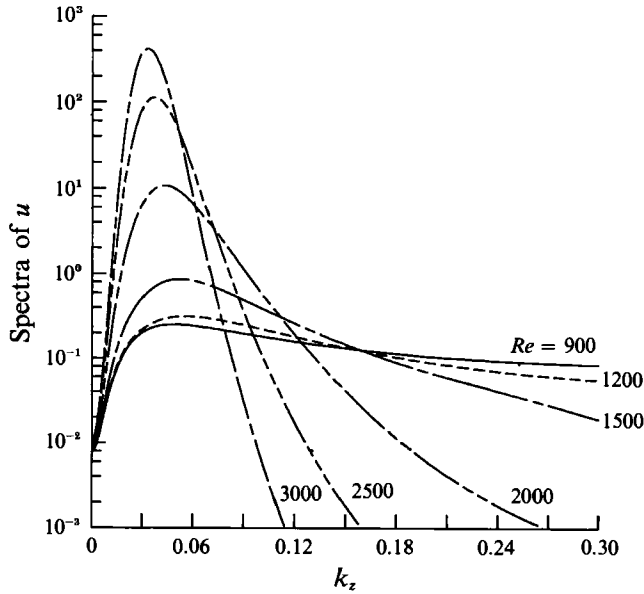
FIGURE 10. Spectra of the u-velocity at several streamwise locations for the Mach 2 case.
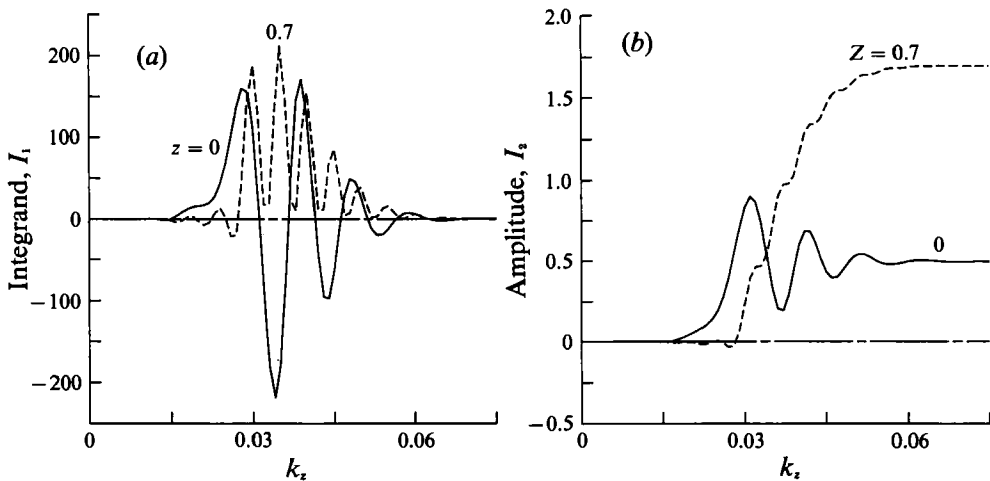

FIGURE 11. (a) the integrand I_1 and (b) the amplitude I_2 in (4.2) for $M = 2$, $F = 0.08 \times 10^{-4}$, $Re = 2900$.

the 0.5° line. The disturbance growth is much larger along the 4° line than along the 0° line. This is because the most amplified oblique modes have group velocity directed at approximately 4°.

Figure 10 shows the spanwise spectrum of the u-velocity at different streamwise locations for Mach number 2. Comparing with figure 6, we note the differences between the spectra for the incompressible and compressible flow. Near the source the amplitude increases with the spanwise wavenumber k_z, peaks near $k_z = 0.05$ and decreases slowly with increasing k_z. With increasing Reynolds number the maximum of the spectrum shifts to a smaller k_z. However, the amplitude of the waves near $k_z = 0$ grows very little. This is because in compressible flows, three-dimensional
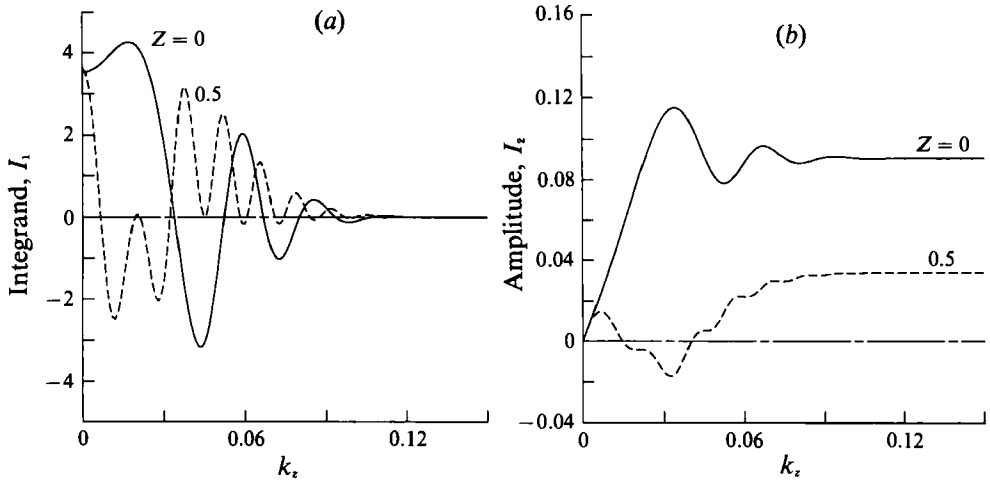
FIGURE 12. (a) Integrand I_1 and (b) the amplitude I_2 in (4.2) for $M = 0$, $F = 0.6 \times 10^{-4}$, $Re = 1095$.

waves grow much more than two-dimensional waves. The shift of the location of the maximum amplitude indicates that the identity of the most amplified wave changes with increasing Reynolds number. The decrease of the width of the spectrum with increasing Reynolds number reflects the spreading of the disturbance in the spanwise direction.

To understand why the maximum amplitude occurs along the centreline for the incompressible case and away from the centreline for the compressible flows we plot the following functions

$$I_1 = (1/\pi) \cos k_z z \, \mathrm{Re}(\tilde{\tilde{I}}) \tag{4.1}$$

and

$$I_2 = \int_0^{k_z} I_1 \, \mathrm{d}k_z. \tag{4.2}$$

We note that I_1 is the integrand in (3.18) and the area under the curve gives the amplitude. Figure 11(a) shows the variation of I_1 with spanwise wavenumber for $M = 2$, at the location $Re = 2900$ and $Z = 0$ and 0.7, while figure 11(b) shows the variation of I_2. Figures 12(a) and 12(b) show the results for $M = 0$, $Re = 1095$ and $Z = 0$ and 0.5. We see that for the incompressible case at $Z = 0$, I_1 is positive and large in the region $k_z < 0.03$ and oscillates beyond $k_z > 0.03$. Hence, the amplitude at $Z = 0$ is contributed by the area under the curve up to $k_z = 0.03$ as evident in figure 12(b). For $Z = 0.5$ we observe that $\cos(k_z z)$ modulates the function I_1, as compared to the $Z = 0$ case, and makes it more oscillatory. Hence, owing to the cancellation of areas of different signs, the amplitude is small away from the centreline. In contrast, for $M = 2$ (figure 11) we see that at $Z = 0$, the function I_1 is oscillatory and, hence, the amplitude is small. At $Z = 0.7$, owing to the modulation by $\cos(k_z z)$, I_1 is shifted to the positive side and hence the area under the curve becomes large.

In figure 13(a), we plot the amplitude ratio, $\log_e(a(x)/a(x = x_0))$, obtained from three different calculations. Curve 1 is obtained from the results of (3.18). The $a(x)$, which is the amplitude of the streamwise velocity component, is obtained by fixing an x-location and selecting the maximum in the spanwise direction. This result is referred to as the non-parallel calculations. The disturbance amplitude at the source,
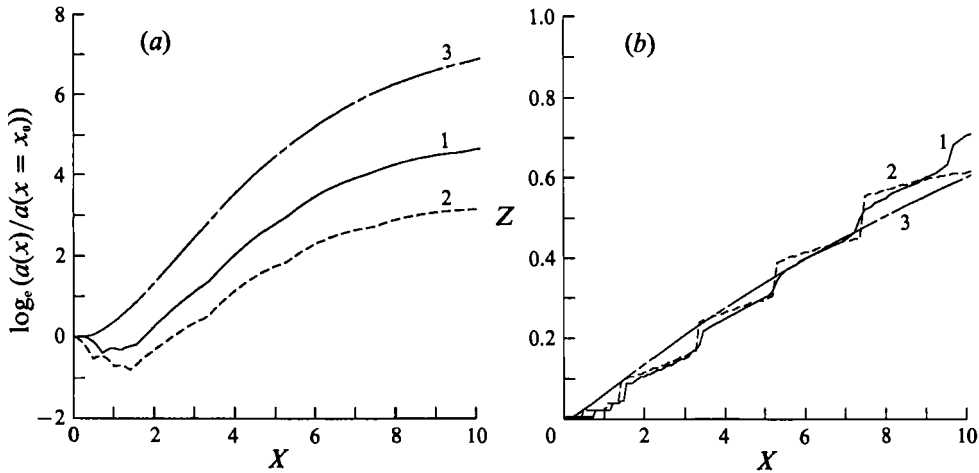
FIGURE 13. (a) Amplitude ratio and (b) locus of maximum amplitude for $M = 2$. Calculations performed using (3.18) (non-parallel) (curve 1), (4.3) (parallel) (curve 2) and most-amplified single normal mode (curve 3).

$a(x = x_0)$, is taken from the receptivity calculations discussed above. Curve 2 is obtained by neglecting the non-parallel effect in the calculation and evaluating the following integral instead of (3.18):

$$\phi = \frac{1}{2\pi} \int e^{ik_z z} \mathrm{Re} \left\{ \exp\left\{ 2i \int_{Re_0}^{Re} \alpha_0 \, dRe - i\omega_0 t \right\} \right\} dk_z. \tag{4.3}$$

This is referred to as results based on parallel theory. Curve 3 is also obtained under the quasi-parallel approximation but the amplitude ratio is computed by using the most-amplified normal mode. Thus, in this case a single mode is used and no interference effect is present.

We see that the single-mode calculation overestimates the amplification of disturbances. For example, logarithmic amplitude ratios at $X = 10$ are 4.5, 3.0 and 6.9 from non-parallel, parallel, and single-mode calculations, respectively. The lower ratios in the parallel and non-parallel calculations are due to the interference effects. If the waves are not in phase, cancellation will occur and the amplification will be less than that for a single wave. We see that when the amplitude is computed from (3.18) or (4.3), there is an initial decay of the disturbance due to wave cancellation. If we match the amplitudes of the parallel and single-mode computations at $X = 1.4$ (where (4.3) shows a minimum), then there is a difference of about 2 in the logarithmic amplitude ratio at the end of the computation. The results from (3.18) and (4.3) also differ due to non-parallel effects, which at this Mach number are significant. In figure 13(b) we have plotted the locus of the maximum amplitude in the (X, Z)-plane and the integration path which is followed in the most-amplified single-mode calculations. It is seen that they all lie close to each other, which shows that the waves grow along the group velocity direction.

4.3. *The Mach 7 case*

Figures 3(c), 4(c), 14 and 15 show the results for $M = 7$, $F = 0.35 \times 10^{-4}$, $Re_0 = 300$. This frequency gives the largest N-factor at the Reynolds number of 3500. For this frequency there exist unstable first and second modes. Up to a Reynolds number of
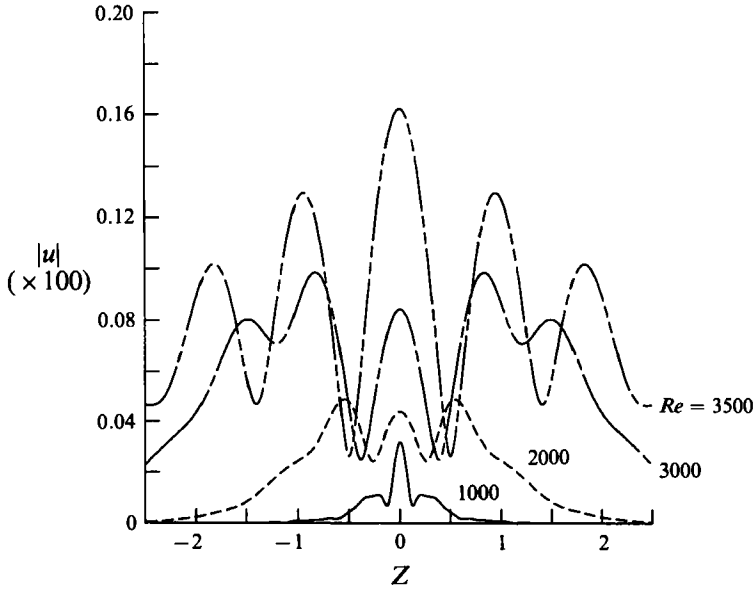
FIGURE 14. Amplitude of the u-velocity at different streamwise locations for the Mach 7 case.
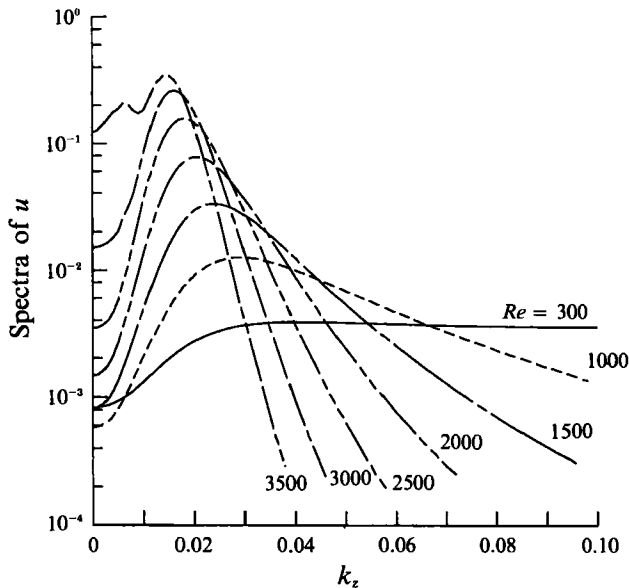

FIGURE 15. Spectra of the u-velocity at several streamwise stations for the Mach 7 case.

about 2500, the disturbances are amplified due to the first mode. The second-mode disturbances are amplified after that Reynolds number. Figure 3(c) shows the u-velocity in the (X, Z)-plane at a height $Y = 18$ and a time t given by $\omega_0 t = 2n\pi$. Figure 4(c) shows the amplitude of the u-velocity in the (X, Z)-plane at the same height. Figure 14 shows the spanwise variation of the amplitude of the u-velocity at the same Y location and at X locations given by $Re = 1000$, 2000, 3000 and 3500. Figure 15 shows the spanwise spectrum of the u-velocity at different streamwise locations.
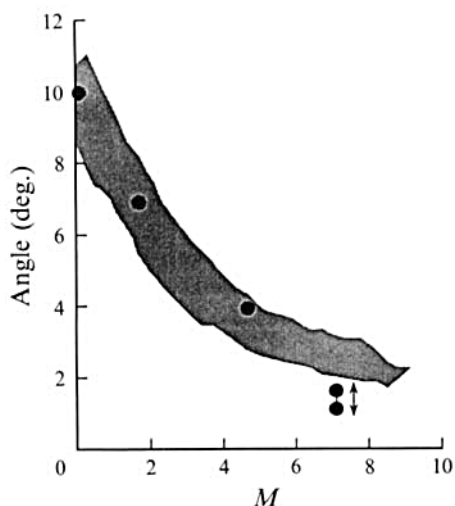
FIGURE 17. Comparison of the computed lateral contamination angle for the instability waves (●) with the lateral turbulence spreading angle obtained experimentally (Fischer 1972) (shaded region).

·First, we observe the differences between the results obtained at the lower Mach number $M = 2$ and the high Mach number $M = 7$. At $M = 7$, the disturbances are amplified along the centreline, as well as along the oblique directions. Up to a Reynolds number of 3000, the amplitudes are larger in the oblique direction than along the centreline. Above a Reynolds number of about 3000, the amplitude along the centreline becomes higher. As explained earlier, this is because the second mode becomes dominant at higher Reynolds numbers. In figure 14, we see that for $Re = 3500$ there exist three peaks between $Z = 0$ and 2.5. It is interesting to note in figure 3 (c) that the angles of the constant phase lines are different in these three peak regions. Along the centreline they are almost two-dimensional, between $Z = 0.5$ and 1.5 they are inclined at $58°$, and beyond that they are inclined at $31°$. In other words, the wave orientation angles are $0°$, $32°$ and $59°$ in the three regions. In the narrow regions where these different constant phase lines merge, we observe the valleys which appear at $Z = 0.5$ and 1.5 for $Re = 3500$ in figures 4 (c) and 14. For this Mach number the lateral spreading angle varies from about $2°$ at low Reynolds number to about $1.5°$ at higher Reynolds number.

The spectra in figure 15 shows the importance of the first and second modes. Even at the high Reynolds number of 3500, the amplitudes for the oblique modes are larger than for the two-dimensional second mode. This shows that, even at high Mach numbers, the first mode remains as important as the second mode. However, the picture would change in the presence of wall cooling, due to its stabilizing effect on the first mode and destabilizing effect on the second mode.

Figure 16 (plate 3) shows the amplitude of the u-velocity in the (Y, Z)-plane for the three different Mach numbers 0, 2 and 7, at X-locations $Re = 1005$, 2900 and 2900 respectively. We again see the splitting of the disturbances in compressible flows when they propagate downstream. We also observe that the critical layer moves towards the edge of the boundary layer with increasing Mach number.

In figure 17, we compare the spreading angles obtained by us with some experimental results for the lateral spread of turbulence (see Fischer 1972). Calculations performed at Mach 4.5 resulted in a half-spreading angle of about $4°$. It

is clear that the spreading angle decreases with the Mach number. The data collected by Fischer are for various sources of disturbances including roughnesses. We see that our results are quite close to the angles found experimentally for the lateral spread of turbulence over a wide range of Mach numbers. It may be that the lateral contamination of turbulence is an instability-related phenomenon or that the region behind the disturbance source in the experiments was in a laminar state.

5. Conclusions

We have investigated the effect of wave interference in supersonic boundary layers. A harmonic point source embedded in the wall introduces disturbances with a given frequency and a wide band of spanwise wavenumbers. The calculations are performed using a direct numerical integration approach and the non-parallel effects are considered by using the method of multiple scales. Results are obtained for Mach numbers $M = 0$, 2 and 7. Mach 2 results are clearly different from the incompressible $M = 0$ results, owing to the effect of compressibility. Additional calculations performed at Mach 4.5 (but not reported here) show that, qualitatively, there is very little difference between the results for $M = 2$ and 4.5, because in both cases first-mode disturbances dominate. At Mach 7, the second-mode disturbance becomes important and, therefore, leaves its distinct mark on the disturbance pattern.

Our results show that, owing to the localized nature of the disturbance, the energy is scattered over a wide band of spanwise wavenumbers. As the waves are amplified downstream of the source, the maximum amplitude occurs away from the centreline. As disturbances propagate further downstream, the maximum amplitude occurs along the centreline in incompressible flows and the three-dimensionality gradually fades away.

In compressible flows at low supersonic Mach numbers, the maximum amplitude occurs along oblique directions in the entire downstream region and the amplitude remains very small along the centreline. At high Mach numbers, the disturbances are amplified both along the centreline and in oblique directions. The two-dimensional second mode eventually takes over, but the amplitude of the oblique first mode remains of comparable order. Wall cooling may change the picture owing to its stabilizing influence on the first mode and destabilizing effect on the second mode.

In all the cases we considered, it is also observed that the growth of the disturbances is weaker than that obtained by following the most-amplified waves. This is due to the mutual interference of different waves. The lower amplitudes found due to wave cancellation do not necessarily mean that the flow is more stable, since various modes generated in the boundary layer can interact nonlinearly, leading to an early breakdown. If only a single mode is excited, it may have to grow to higher amplitudes before secondary instabilities can develop from background disturbances.

We also observe that the disturbances spread in wedge-shaped regions behind the source and the wedge angle decreases with the Mach number. At Mach numbers of 0, 2 and 4.5, the lateral spreading half-angles are found to be about 10°, 7° and 4°, respectively. The spreading angle for the Mach 7 case is between 1.5° and 2° depending upon the Reynolds number. Since disturbance energy propagates in the group velocity direction, these spreading angles are associated with the highest group velocity angles for the oblique unstable waves, which may change somewhat with the frequency. It is also observed that these lateral spreading angles are quite close to the angles found experimentally for the lateral spread of turbulence over a wide range of Mach numbers.

REFERENCES

BALAKUMAR, P. & MALIK, M. R. 1992 *J. Fluid Mech.* **239**, 631 (referred to herein as BM).

EL-HADY, N. M. 1991 *AIAA Paper* 91-0324.

FISCHER, M. C. 1972 *AIAA J.* **10**,

GAPANOV, S. A. 1981 *Proc. Eighth Canadian Cong. of Appl. Mech.*, p. 673.

GASTER, M. 1982 *Proc. R. Soc. Lond.* A **384**, 317.

GASTER, M. & GRANT, I. 1975 *Proc. R. Soc. Lond.* A **347**, 253.

GILEV, B. M., KACHANOV, YU, S. & KOZLOV, V. V. 1981 *Novosibirsk*, 46. (Preprint/AN SSSR, Sib. Division, ITPM; 34.)

KOSINOV, A. B. & MASLOV, A. A. 1985 In *Laminar-Turbulent Transition* (ed. V. V. Kozlov), p. 601. Springer.

KOSINOV, A. D., MASLOV, A. A. & SHEVELKOV, S. G. 1990 *J. Fluid Mech.* **219**, 621.

MACK, L. M. 1985 In *Laminar-Turbulent Transition* (ed. V. V. Kozlov), p. 125. Springer.

MACK, L. M. & KENDALL, J. M. 1983 *AIAA Paper* 83-0046.

MALIK, M. R. 1990 *J. Comput. Phys.* **86**, 376.

MALIK, M. R., CHUANG, S. & HUSSAINI, M. Y. 1982 *Z. Angew. Math. Phys.* **33**, 189.

SARIC, W. S. & NAYFEH, A. H. 1975 *Phys. Fluids* **18**, 945.